

## Nonlinear optical microscopy improvement by focal-point axial modulation

Mahdi Mozdoor Dashtabi  
Reza Massudi

# Nonlinear optical microscopy improvement by focal-point axial modulation

Mahdi Mozdoor Dashtabi and Reza Massudi\*

Shahid Beheshti University, G.C., Laser and Plasma Research Institute, Evin, Tehran 1983969411, Iran

**Abstract.** Among the most important challenges of microscopy—even more important than the resolution enhancement, especially in biological and neuroscience applications—is noninvasive and label-free imaging deeper into live scattering samples. However, the fundamental limitation on imaging depth is the signal-to-background ratio in scattering biological tissues. Here, using a vibrating microscope objective in conjunction with a lock-in amplifier, we demonstrate the background cancellation in imaging the samples surrounded by turbid and scattering media, which leads to more clear images deeper into the samples. Furthermore, this technique offers the localization and resolution enhancement as well as resolves ambiguities in signal interpretation, using a single-color laser. This technique is applicable to most nonlinear as well as some linear point-scanning optical microscopies. © 2016 Society of Photo-Optical Instrumentation Engineers (SPIE) [DOI: 10.1117/1.JBO.21.5.056006]

**Keywords:** third-harmonic-generation microscopy; multiphoton microscopy; nonlinear optical microscopy; laser scanning microscopy; bioimaging.

Paper 160034LRR received Jan. 18, 2016; accepted for publication Apr. 27, 2016; published online May 26, 2016.

## 1 Introduction

The emergence of nonlinear optics has led to tremendous improvements in optical microscopy. Different nonlinear optical microscopy (NOM) techniques, such as two-photon excitation fluorescence,<sup>1,2</sup> second-harmonic generation (SHG),<sup>3–5</sup> third-harmonic generation (THG),<sup>6–11</sup> nonlinear photothermal and photoacoustic,<sup>12–14</sup> and Raman scattering,<sup>2,15,16</sup> have been developed to overcome some drawbacks of linear optical microscopy.

NOM, in addition to increasing the resolution, has the ability to image deeper into the samples compared to linear optical microscopy when near-infrared (NIR) excitation is employed,<sup>17–19</sup> because using NIR excitation reduces the scattering and the optical absorption in biological systems. Scattering in samples leads to a background that reduces the signal-to-background ratio (SBR) and, as a result, blurs the deep images and decreases the resolution. Furthermore, using NIR becomes less likely to reduce the cell viability<sup>11</sup> as compared to shorter wavelengths, because of the reduced out-of-focus absorption.<sup>20</sup> Although exploiting longer wavelengths results in reduced scattering and generated background,<sup>18</sup> the level of SBR is still low, which limits the maximum attainable imaging depth. On the other hand, in NOM, the signal is generated only in the regions with significant pump intensities, and, consequently, optical sectioning can take place when a tightly focused excitation laser beam is employed. However, despite the ability to overcome the diffraction-limited lateral resolution due to the nonlinearity of the imaging process,<sup>12–14,21</sup> the axial resolution in most of these techniques is not yet sufficient for optical sectioning in some applications. To enhance the axial resolution, a few techniques<sup>22,23</sup> have been reported; however, they suffer from various problems such as the need for multi-color pulses, complex and expensive setups, and/or being appropriate only for surface topography measurements.

To circumvent some of these drawbacks, we propose the modulation-detection technique or, in other words, derivative-detection

technique. Its main advantage is phase-sensitive detection capability, which is used to limit the response of the detection system to a narrow interval centered at the modulation frequency. Furthermore, a frequency-independent background signal and background noise are essentially reduced, resulting in a higher signal-to-noise ratio, which makes this method superior to intensity-modulation techniques.<sup>24</sup> This method, while preserving all its advantages, can also be translated into spatial domain, where it can be implemented to point-scanning NOMs to boost their performance.

In this study, we introduce the focal-point axial modulation nonlinear optical microscopy (FPAM-NOM) and use it to improve THG microscopy using a single-color laser. We exploit its advantage to cancel out the background generated by turbid media surrounding the sample, to enhance the axial resolution and the localization, and also to resolve ambiguities in signal interpretation. Finally, since FPAM-NOM is based on the nonlinear optical properties of materials, it can be applied to label-free imaging for biological applications.

## 2 Focal-Point Axial Modulation Nonlinear Optical Microscopy Principle

In FPAM-NOM, location of the focal point is modulated by a distance of  $2\delta_0$  along the  $z$ -axis with a modulation frequency of  $f$  [Figs. 1(a)–1(c)]. Consequently, the generated third-harmonic signal is also modulated, so that the THG signal before the detector in the cylindrical coordinate is

$$I_S(z, t) = \int_0^{+\infty} I^3[\rho, z + \delta_0 \sin(2\pi f t)] d\rho, \quad (1)$$

where  $\rho$  and  $z$  are the cylindrical coordinate components and  $I$  is the fundamental harmonic intensity. Equation (1) shows that the detected signal is modulated by time for a specified  $z$ . The  $f$  frequency component of  $I_S$  and  $S_f(z)$ , acquired by passing the electrical signal of the detector through a lock-in amplifier

\*Address all correspondence to: Reza Massudi, E-mail: r-massudi@sbu.ac.ir

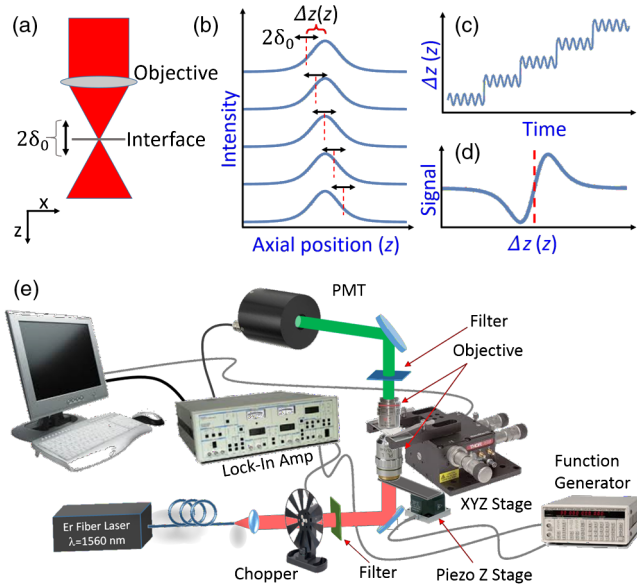


**Fig. 1** Principle of FPAM-NOM and experimental setup. (a) Modulation of an interface inside the sample relative to the focal point along the axial direction with a modulation depth of  $2\delta_0$ . (b) Scanning the axial position of the modulating focal point along the  $z$ -direction relative to the interface-generated THG signal inside the sample. (c) Position of the interface relative to the focal point along the axial direction versus time. (d) Generated signal after lock-in amplifier versus the axial position of the interface relative to the focal point. The red vertical dashed lines represent the interface. (e) THG microscopy setup. In a conventional experiment, the chopper is on and the piezo-stage is off, while in the FPAM-NOM setup, the chopper is removed and the piezo-stage is on. In this study,  $\delta_0 = 1 \mu\text{m}$ , and frequencies of the chopper and the function generator are 249.3.

locked at frequency  $f$ , is proportional to the first derivative of  $I_S(z)$  with respect to  $z$  [Fig. 1(d)].<sup>24</sup>

In principle, THG is more significant when the interfaces of the sample under study are located within one confocal parameter from the focal plane,<sup>21</sup> which itself provides some inherent sectioning.<sup>8,14</sup> However, in conventional THG microscopy, interpretation of the signal comes with some ambiguities. That is because it is not clear whether any change in the level of the signal is related to the variation of the axial distance of the interface from focus in negative or positive  $z$ -direction, or it comes from a possible variation of the material properties. But in FPAM technique, the sign of  $S_f(z)$  changes when the focus traverses the interface [Fig. 1(d)], and, hence, the location of the sectioning plane (focal plane) and also the  $z$ -direction of the interface can be precisely determined. Consequently, by comparison of the data obtained from the two methods (conventional and FPAM), one can conclude whether the change in the detected signal is due to the variation in the material property or the interface-sectioning plane distance. Furthermore, as the FPAM signal [Fig. 1(d)] varies linearly as a function of  $z$  around the interface ( $\Delta z = 0$ ), it could be used for optical sectioning and localization.<sup>25,26</sup>

### 3 Materials and Methods

#### 3.1 Imaging Setup

The experimental setup for the conventional and FPAM-NOM THG microscopies is shown in Fig. 1(e). We employ a home-made, all-fiber, mode-locked, Er-doped oscillator-amplifier

delivering 200 fs pulses at 1570 nm with the repetition rate of 20 MHz and maximum average power of 230 mW. A 40× air objective (0.65 NA) is used to focus the laser into the sample. As the nonlinear THG signal is very weak, because of low conversion efficiency (lower than  $10^{-5}$ ),<sup>8</sup> it is detected by a photomultiplier tube (PMT, Hamamatsu, R329-02) through a lock-in amplifier (Stanford Research Systems, SR530). To exclude the wavelengths other than those of the excitation laser and the THG, optical filters are placed before the focusing objective and in-front of the PMT, respectively.

The conventional setup for THG microscopy [Fig. 1(e)] benefits from a lock-in amplifier in conjunction with an optical chopper (Newport, 3501) as noise-rejection elements. To convert the conventional setup of Fig. 1(e) to FPAM-NOM, the chopper is replaced with a piezo-actuator with 20-nm resolution (Melles Griot, NanoMax-TS) together with a function generator (Stanford Research Systems, DS345), which drives the focusing objectives to oscillate along the optical axis, thus modulating the focal position inside the sample. The modulation frequency  $f$  in the FPAM-NOM setup is 249.3 Hz, which is limited by the frequency response of the piezoelectric transducer stage, and the modulation depth of focus  $\delta_0$  is  $1 \mu\text{m}$ , which is measured through the sensor port of the piezo-actuator. To make the data acquired by two setups comparable, the chopper modulation frequency is also set to 249.3 Hz. To avoid the possible small phase drift due to the resonant oscillation of the objective, the reference signal of the lock-in amplifier is taken from the sensor output port of the piezo-actuator. Controlling the components and data acquisition is performed through general purpose interface bus port and data processing, and image generation is performed using a code written in Mathematica.

#### 3.2 Image Formation

The third-harmonic images are synthesized through point-by-point measurement with the sample scanned by a stepper motor stage with 25-nm resolution (Melles Griot, NanoMax-HS). THG images of the red blood cell (RBC) are acquired by the XYZ stepper motor stage scanned with step sizes of  $1 \mu\text{m}$  along the  $z$ -axis and step sizes of 200 nm along the  $x$ - and  $y$ -axes. In this setup, the laser beam enters from the bottom and the PMT is located on top of the sample. Hence, in scanning along the  $z$ -axis, moving toward the laser leads to more negative  $z$ . Therefore, the left peak in Figs. 2(a), 2(g), and 2(h) corresponds to the coverslip's side toward the PMT and far from the laser (deeper within the sample).

#### 3.3 Sample Preparation

The blood smear was prepared using fresh blood, without any anticoagulant, on a coverslip. Fixation of the thin smear was done with anhydrous methanol for 1 to 2 min, after which the slides were air-dried.

To prepare the egg-white sample, a droplet of fresh egg-white is dripped on a coverslip, and the second coverslip is placed on it. It is then placed into an oven for a few seconds.

#### 3.4 Axial-Resolution Calculation

To calculate the axial-resolution enhancement, images of a wedge that is formed using two coverslips with immersion oil in between are taken using both techniques. FPAM data are acquired with  $1 \mu\text{m}$  of modulation depth of focus  $\delta_0$  and  $1 \mu\text{m}$

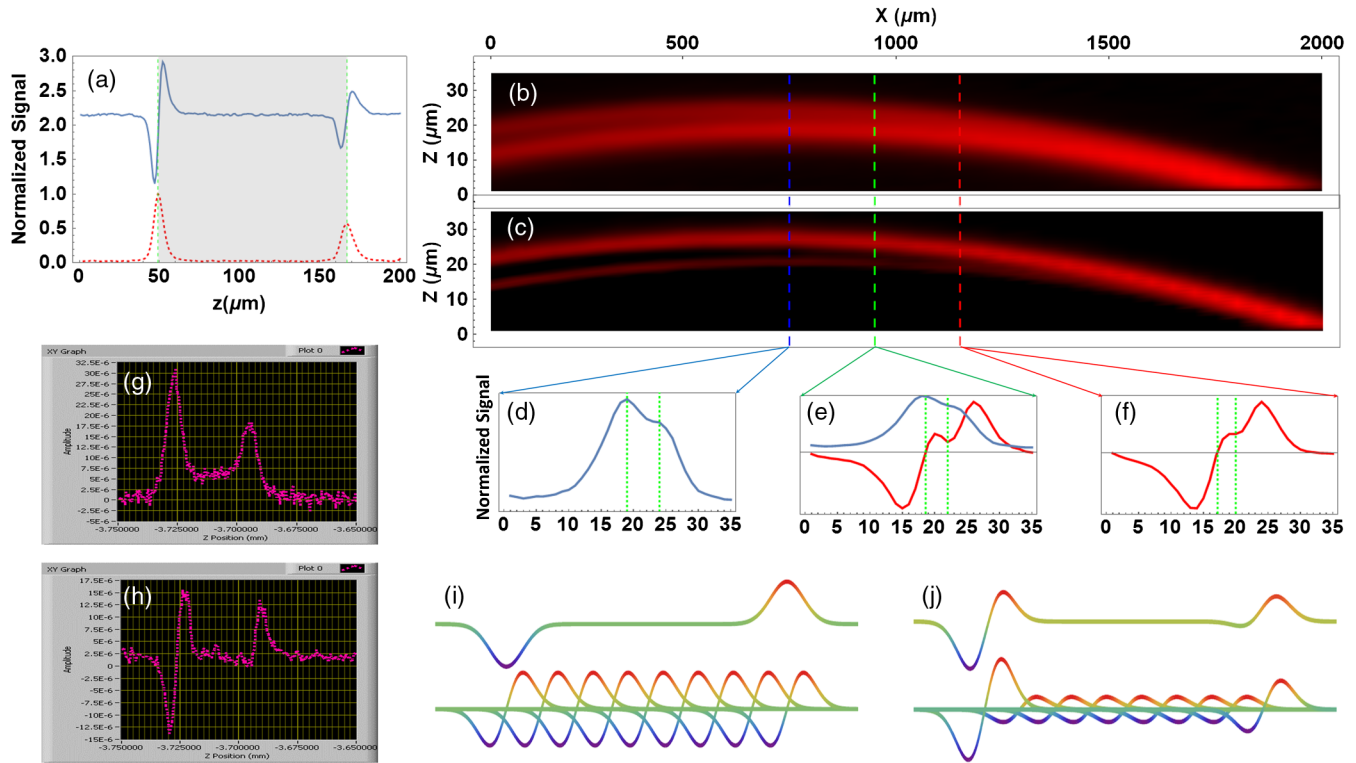


**Fig. 2** Conventional and FPAM-NOM THG microscopy signals of axially scanned samples. (a) THG microscopy signal of a coverslip using conventional (dashed line) and FPAM-NOM (solid line) setups. Gray area shows the coverslip. THG image of a wedge with (b) conventional and (c) FPAM-NOM methods. Raw data in place of the maximum resolving limits of (d) the former and (f) the later techniques correspond to blue and red dashed lines in (b) and (c), respectively. (e) A point between the two maximum resolving limits of the two methods. THG generated from a thin layer of baked egg-white sandwiched between two coverslips using (g) conventional and (h) FPAM-NOM techniques. The principle of background cancellation (i) in only turbid media and (j) the numerical reconstruction of it in the media including baked egg-white sandwiched between two coverslips corresponding to (h). The vertical dashed lines in (d)–(f) illustrate the glass–oil interfaces acquired from corresponding data.

of the XYZ stage  $z$ -axis steps in the  $x - z$  plane. The distance between the two interfaces is acquired every  $50 \mu\text{m}$  along the  $x$ -axis, and the axial resolution is calculated after the data interpolation. It should be noted that due to the imperfection in the orthogonality of the XYZ stage, as it incorporates parallel flexure as travel mechanism, the wedge looks curved. In the other words, the stage (on long distances) travels on a circular path instead of a straight line. Such curvature is exaggerated in Figs. 2(b) and 2(c) due to the different scales of the  $x$ - and  $y$ -axes.

### 3.5 Signal-to-Background Ratio Calculation

The value of SBR for each peak is calculated by dividing the absolute value of that peak to the average value of the signal over a specified region inside the egg-white layer. Since the observed signal [Figs. 2(g) and 2(h)] is the superposition of two separate peaks, namely, the background and the noise, the location for the background is defined far enough from those peaks to minimize the contribution of their tails. In other words, such location is chosen where the value of the signal and noise is smaller than that in the middle of the egg-white layer in the conventional data.

## 4 Results and Discussion

Figure 2(a) shows the signals acquired by conventional (dashed line) and FPAM-THG (solid line) techniques from glass–air

interfaces by scanning a coverslip along its surface normal. As is evident, FPAM-NOM signal (solid line) is proportional to the first derivative of the signal of the conventional setup (dashed line) with respect to  $z$ . The two peaks with  $120\text{-}\mu\text{m}$  distance correspond to the surfaces of the coverslip.

To verify the axial-resolution enhancement by FPAM-NOM, the images from the  $xz$  plane of a wedge are taken using conventional [Fig. 2(b)] and FPAM-NOM [Fig. 2(c)] techniques. Figures 2(d) and 2(f) show the corresponding detected signal profiles along the left and the right dashed lines in Figs. 2(b) and 2(c), respectively. They represent the maximum resolving limits of conventional and FPAM-NOM techniques, respectively. Figure 2(e) shows the detected signal for the central dashed line to compare the acquired signal by the two techniques for a point located between the two maximum resolution limits. The best axial resolutions achieved using conventional and FPAM-NOM methods are  $5$  and  $2.8 \mu\text{m}$ , respectively, which shows an enhancement of about  $1.8$  times. We expect further improvement of the axial resolution and the enhancement factor using, respectively, objectives with higher numerical aperture and higher harmonic detection modes of the lock-in amplifier.<sup>24</sup>

Another interesting advantage of FPAM-NOM, which originates from its derivative nature, occurs in imaging of a sample within a turbid medium, such as a brain, in which the distance between the interfaces of its components (e.g., cell dendrites and organelles) is shorter than the axial resolving power. In such



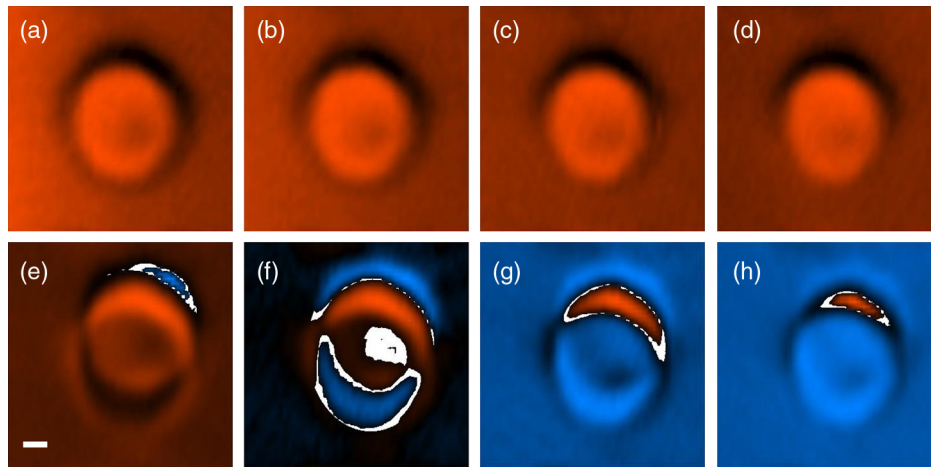


**Fig. 3** THG images of an RBC. Normalized  $x - y$  frames of (a)–(d) conventional and (e)–(h) FPAM-NOM techniques. The blue area shows the sample interfaces below the scanning plane, while the red area represents those above it. For convenience, the blue and red regions were individually normalized. All frames have  $1 \mu\text{m}$  of axial distance from each other. For convenience, the intersections of the sample with the scanning planes are illustrated by white. Scale bar:  $1 \mu\text{m}$ .

media, imaging by a conventional technique generates a significant level of signal from the surrounding media [Fig. 2(g)]. This signal acts as a background, blurring the sample edges. Employing FPAM-NOM eliminates such background and generates high-contrast images [Fig. 2(h)]. To verify this, a thin layer of baked egg-white (turbid medium) sandwiched between two coverslips (sample) is used and scanned along the  $z$ -axis.

As is evident, in FPAM-NOM, unlike the conventional setup [Fig. 2(g)], the THG signal from the egg-white layer (the background signal) is eliminated from the detected signal, and accordingly, the interfaces of the coverslips become more visible, and SBR increases as well [Fig. 2(h)]. The achieved peak of the SBR enhancement factor, here, is about 25.3. Note that this background is the signal generated by the turbid media and cannot be canceled by nonderivative techniques. The reason of such enhancement can be explained as follows: the egg-white layer can be considered as a stack of infinitely thin slabs, each generating a THG signal. In normal NOM method, they add up and contribute to the background signal. However, in FPAM-NOM, the THG signals generated from the adjacent slabs cancel out each other. Such cancellation is due to the derivative nature of those signals [Fig. 2(i)], and, therefore, no background from the turbid media is observed in the signal. By this explanation, we can interpret the signal in Fig. 2(h) as a superposition of the signals from the two glass/egg-white interfaces and that from the turbid media, which is numerically reconstructed and is shown in Fig. 2(j). It is interesting to note that although the right peak (deeper sample interface) is less intense than the left one, its SBR enhancement factor is bigger (25.3 against 20.1), which implies that the depth-dependent signal attenuation is less pronounced in FPAM as compared to a conventional method.

Finally, to show the localization enhancement and resolving ambiguities by FPAM, the images of an RBC are acquired and compared with that acquired by conventional THG microscopy. As can be seen in Fig. 3, while the conventional images cannot resolve the axial displacement of  $4 \mu\text{m}$  among the four frames [Figs. 3(a)–3(d)], the FPAM technique can well resolve the sample points, which are below (blue) or above (red) the scanning plane [Figs. 3(e)–3(h)]. Hence, as the scanning plane moves toward the top of the cell, the blue region increases

and the size of the red area reduces. The image also shows that the RBC is placed obliquely relative to the coverslip surface [Figs. 3(e)–3(h)], which is difficult, or even impossible, to be recognized with most other techniques.

Such features of FPAM-NOM result in better resolved images with sharper edges from samples inside turbid media, which makes it advantageous for applications such as brain imaging. Furthermore, one can use the signals before and after the lock-in amplifier to benefit from the advantages of conventional and FPAM techniques simultaneously. Finally, although this report is dedicated to THG microscopy, FPAM-NOM is also applicable to some other NOMs, e.g., SHG.

## References

1. P. Mahou et al., "Multicolor two-photon light-sheet microscopy," *Nat. Methods* **11**, 600–601 (2014).
2. C.-H. Chien et al., "Label-free imaging of *Drosophila* in vivo by coherent anti-Stokes Raman scattering and two-photon excitation autofluorescence microscopy," *J. Biomed. Opt.* **16**(1), 016012 (2011).
3. P. J. Campagnola and C.-Y. Dong, "Second harmonic generation microscopy: principles and applications to disease diagnosis," *Laser Photonics Rev.* **5**(1), 13–26 (2011).
4. J. Liu et al., "Single-cell screening and quantification of transcripts in cancer tissues by second-harmonic generation microscopy," *J. Biomed. Opt.* **20**(9), 96016 (2015).
5. N. Morishige et al., "Quantitative analysis of collagen lamellae in the normal and keratoconic human cornea by second harmonic generation imaging microscopy," *Invest. Ophthalmol. Visual Sci.* **55**(12), 8377–8385 (2014).
6. J. Lin et al., "Label-free three-dimensional imaging of cell nucleus using third-harmonic generation microscopy," *Appl. Phys. Lett.* **105**(10), 103705 (2014).
7. G. J. Tservelakis et al., "Cell tracking in live *Caenorhabditis elegans* embryos via third harmonic generation imaging microscopy measurements," *J. Biomed. Opt.* **16**(4), 046019 (2011).
8. A. C. Millard et al., "Third-harmonic generation microscopy by use of a compact, femtosecond fiber laser source," *Appl. Opt.* **38**(36), 7393–7397 (1999).
9. Y.-C. Chen et al., "Third-harmonic generation microscopy reveals dental anatomy in ancient fossils," *Opt. Lett.* **40**, 1354–1357 (2015).
10. M. Zimmerley et al., "Probing ordered lipid assemblies with polarized third-harmonic-generation microscopy," *Phys. Rev. X* **3**, 11002 (2013).

11. E. Gavgiotaki et al., "Third harmonic generation microscopy as a reliable diagnostic tool for evaluating lipid body modification during cell activation: the example of BV-2 microglia cells," *J. Struct. Biol.* **189**(2), 105–113 (2015).
12. D. A. Nedosekin et al., "Super-resolution nonlinear photothermal microscopy," *Small* **10**(1), 135–142 (2014).
13. V. P. Zharov, "Ultrasharp nonlinear photothermal and photoacoustic resonances and holes beyond the spectral limit," *Nat. Photonics* **5**(2), 110–116 (2011).
14. J. Yao et al., "Photoimprint photoacoustic microscopy for three-dimensional label-free subdiffraction imaging," *Phys. Rev. Lett.* **112**, 014302 (2014).
15. P. C. Christophersen et al., "Investigation of protein distribution in solid lipid particles and its impact on protein release using coherent anti-Stokes Raman scattering microscopy," *J. Controlled Release* **197**, 111–120 (2015).
16. H. Tu and S. A. Boppart, "Coherent anti-Stokes Raman scattering microscopy: overcoming technical barriers for clinical translation," *J. Biophotonics* **7**(1–2), 9–22 (2014).
17. E. E. Hoover and J. A. Squier, "Advances in multiphoton microscopy technology," *Nat. Photonics* **7**, 93–101 (2013).
18. N. G. Horton et al., "In vivo three-photon microscopy of subcortical structures within an intact mouse brain," *Nat. Photonics* **7**, 205–209 (2013).
19. M. Yildirim, N. Durr, and A. Ben-Yakar, "Tripling the maximum imaging depth with third-harmonic generation microscopy," *J. Biomed. Opt.* **20**(9), 096013 (2015).
20. J. Squier et al., "Characterization of femtosecond pulses focused with high numerical aperture optics using interferometric surface-third-harmonic generation," *Opt. Commun.* **147**, 153–156 (1998).
21. J. Squier and M. Müller, "High resolution nonlinear microscopy: a review of sources and methods for achieving optimal imaging," *Rev. Sci. Instrum.* **72**(7), 2855–2867 (2001).
22. K. Isobe et al., "Background-free deep imaging by spatial overlap modulation nonlinear optical microscopy," *Biomed. Opt. Express* **3**(7), 1594 (2012).
23. D. Sandkuijl et al., "Interferometric backward third harmonic generation microscopy for axial imaging with accuracy beyond the diffraction limit," *PLoS One* **9**(4), e94458 (2014).
24. W. Demtröder, *Laser Spectroscopy 2—Experimental Techniques*, Springer, Berlin Heidelberg (2015).
25. F. Chasles, B. Dubertret, and A. C. Boccara, "Full-field optical sectioning and three-dimensional localization of fluorescent particles using focal plane modulation," *Opt. Lett.* **31**(9), 1274–1276 (2006).
26. V. Levi, Q. Ruan, and E. Gratton, "3-D particle tracking in a two-photon microscope: application to the study of molecular dynamics in cells," *Biophys. J.* **88**(4), 2919–2928 (2005).